Comparison of continuous and discontinuous Galerkin approaches for variable-viscosity Stokes flow

Ragnar S. Lehmann[1,2,*], **Mária Lukáčová-Medvid'ová**[1,3], **Boris J. P. Kaus**[1,2], and **Anton A. Popov**[2]

[1] Max Planck Graduate Center with the Johannes Gutenberg-Universität Mainz (MPGC), Germany

[2] Institute of Geosciences, Johannes Gutenberg-Universität Mainz, Germany

[3] Institute of Mathematics, Johannes Gutenberg-Universität Mainz, Germany

We describe a Discontinuous Galerkin (DG) scheme for variable-viscosity Stokes flow which is a crucial aspect of many geophysical modelling applications and conduct numerical experiments with different elements comparing the DG approach to the standard Finite Element Method (FEM). We compare the divergence-conforming lowest-order Raviart-Thomas (RT_0P_0) and Brezzi-Douglas-Marini (BDM_1P_0) element in the DG scheme with the bilinear Q_1P_0 and biquadratic Q_2P_1 elements for velocity and their matching piecewise constant/linear elements for pressure in the standard continuous Galerkin (CG) scheme with respect to accuracy and memory usage in 2D benchmark setups.

We find that for the chosen geodynamic benchmark setups the DG scheme with the BDM_1P_0 element gives the expected convergence rates and accuracy but has (for fixed mesh) higher memory requirements than the CG scheme with the Q_1P_0 element without yielding significantly higher accuracy. The DG scheme with the RT_0P_0 element is cheaper than the other first-order elements and yields almost the same accuracy in simple cases but does not converge for setups with non-zero shear stress. The known instability modes of the Q_1P_0 element did not play a role in the tested setups leading to the BDM_1P_0 and Q_1P_0 elements being equally reliable. Not only for a fixed mesh resolution, but also for fixed memory limitations, using a second-order element like Q_2P_1 gives higher accuracy than the considered first-order elements.

© 2015 WILEY-VCH Verlag GmbH & Co. KGaA, Weinheim

1 Introduction and geophysical motivation

Numerical simulations of geological and geodynamic processes is an important and growing research field which helps to interpret geological observations in a physically meaningful manner. Typical questions that are addressed include: How are sedimentary basins formed (e.g., [1])? How do lithospheric plates collide and how are mountains formed (e.g., [2–5])? Why do we have plate tectonics on Earth and not on other planets (e.g., [6,7])? What is the rheology of magma [8] and how does magma move through the Earth and why does it only sometimes result in volcanic eruptions [9]? How does mantle convection work [7], and was this different in the early Earth [10]? While the rheology of rocks is rather complex and nonlinear and is best described as viscoelastoplastic, inertial terms are not important for these processes and the governing equations that need to be solved in this case are often very similar to the incompressible Stokes equations [7, 11–14]. Yet, different than in many classical CFD applications, geological processes have viscosities that vary by many orders of magnitude over spatially small domains as the viscosity of rocks depends on pressure, temperature, strain rate. The location of these viscosity jumps are typically not known a-priori but might form spontaneously during a simulation, for example when a plastic shear band forms [15]. Obviously, geodynamic models need to capture these variations, see, e.g., [9, 16, 17]. The reliability of the numerical method is influenced by its stability and accuracy for the case of discontinuous model parameters, cf. [18, 19].

Most geodynamic models contain a Stokes flow component, e.g. [20–22], as typical time scales are long, inertial effects are negligible and rocks can often be considered nearly incompressible. Therefore, finding a good way of solving the Stokes system is likely to contribute to a better understanding of, e.g., mantle convection, subduction of tectonic plates or continental collision. The choice of the discretization method represents the first step in that solution process. Grid-based methods such as finite differences [12, 23], finite elements and finite volumes [24] are predominantly used. Each of these methods algebraically yields a saddle point problem with a coefficient matrix that is, typically, very large, ill-conditioned and indefinite [25]. Particularly for solving 3D problems, massively parallel systems need to be solved, for which iterative

---

* Corresponding author E-mail: r.lehmann@uni-mainz.de

methods are crucial although finding fast methods is still an open question, cf. [26]. We refer to recent works dealing with block preconditioning with algebraic multigrid [25, 27, 28], Krylov subspace methods on decoupled and fully coupled systems [22, 29] and projection-based preconditioners [30, 31].

The Finite Element Method (FEM) is one of the standard means for the simulation of geodynamic processes used in, e.g., [32–37]. However, the "natural" trade-off between accuracy and computational expenses accounts for searching enhanced methods. As discontinuous Galerkin methods have been demonstrated to be very efficient for solving (seismic) wave propagation in heterogeneous media [38], they might be as useful for solving variable viscosity Stokes problems as well. Our aim is therefore to test how the Continuous Galerkin (CG) and the Discontinuous Galerkin (DG) methods compare with the two most commonly used quadrilateral elements for Stokes flow (Q_1P_0 and Q_2P_1). We do not consider the Q_1Q_1/stab element [39–41], as stabilization of this element is achieved by introducing an artificial compressibility that dominates for flows mainly driven by buoyancy variations [37]. In geophysical flow models this yields unphysical pressure artifacts for cases where both the free surface of the Earth and mantle flow are considered, because the driving density contrast between cold sinking plates and the warmer surrounding Earth's mantle is much smaller than the density difference between rocks and air [15, 35, 36]. In our experience, this results in artificial "compaction" of the Earth's mantle if Q_1Q_1/stab element is used, which makes them unsuitable for these purposes.

The DG method generalizes the FEM by eliminating continuity constraints and providing the tools to handle potential jumps via numerical fluxes. In this respect it transfers a classical advantage of the finite volume methods to a finite element approach [42]. Hence, it provides additional flexibility in designing the shape functions that are discontinuous, and means to stabilize discontinuities or steep gradient regions. DG methods are inherently local requiring less communication between neighbouring mesh cells. This facilitates the enforcement of local mass conservation (i.e., per mesh cell) [43–45], the development of multiscale methods [46], hp-adaptivity [47, 48] and parallelization [49, 50]. On the other hand, DG methods yield additional degrees of freedom compared to CG.

Since about two decades DG methods have become increasingly popular in the mathematical community [51, 52] and are tested and used more and more in different fields of applications. Geophysical applications using DG methods are hitherto mainly restricted to seismology (wave modelling, waveform inversion), see, e.g., [38, 53, 54]. Wilcox *et al.* give as reasons for employing a DG method (among others) strong wave speed contrasts and the need for h-adaptive non-conforming meshes to track solution features [38]. Although steep gradients and discontinuities are present in solutions and material properties of typical geodynamic models, so far DG methods have not been applied to common geodynamic model benchmarks. The aim of this paper is to realize a first step in this direction. We employ $H(\mathrm{div})$-conforming elements of Raviart-Thomas and of Brezzi-Douglas-Marini kind. Thus, the velocity approximation is globally divergence free in the Sobolev space H^1, cf. (4c). It is a well-known fact that exactly divergence-free basis functions can be advantageous for the approximation of the Navier-Stokes and Darcy flows, see, e.g., [55, 56].

This article is organized as follows: in Sect. 2 we give a brief review on the main differences between CG and DG methods, present the elements, show the derivation of a DG scheme for the Stokes flow, and describe the benchmark setups we used in the numerical experiments. In particular, we enforce local mass conservation by preserving the divergence-free condition using div-conforming approximation for velocities in our DG scheme as described in Sect. 2.3. In Sect. 3 we confer the results of the benchmark setups and the computational costs arising from the different elements and schemes. Finally, these results are discussed and conclusions are drawn.

2   Derivation of the numerical method

2.1   Governing equations

Stokes flow plays a major role in geodynamic processes like, e.g., mantle convection. It is also called creeping motion describing a flow where viscous forces dominate over inertial forces. If the material is assumed to be incompressible, Stokes flow can be described by the following conservation laws of momentum and mass:

$$-\nabla \cdot \boldsymbol{\tau} + \nabla p = -\rho g \hat{\mathbf{z}}, \tag{1a}$$

$$\nabla \cdot \boldsymbol{v} = 0, \tag{1b}$$

where $\boldsymbol{v}$ denotes velocity, p pressure, $\boldsymbol{\tau}$ the deviatoric stress tensor, ρ density, g the gravitational acceleration, and $\hat{\mathbf{z}}$ the unity vector pointing in (vertical) z direction. The equation of state specifying the deviatoric stress $\boldsymbol{\tau}$ completes the system,

$$\boldsymbol{\tau} = 2\mu \dot{\boldsymbol{\epsilon}} \tag{2}$$

where μ denotes the viscosity and $\dot{\boldsymbol{\epsilon}} \equiv \dot{\boldsymbol{\epsilon}}(\boldsymbol{v}) = \frac{1}{2}(\nabla\boldsymbol{v} + \nabla\boldsymbol{v}^{\mathsf{T}})$ the strain rate. In the following, we only consider the 2D case with (x, z) coordinates and the following boundary conditions,

$$\text{Free-slip:} \quad \boldsymbol{v} \cdot \boldsymbol{n} = 0, \quad \frac{\partial \boldsymbol{v}}{\partial \boldsymbol{n}} = 0 \quad \text{on } \Gamma_1 \subset \partial\Omega, \tag{3a}$$

$$\text{No-slip:} \quad \boldsymbol{v} = 0 \quad\quad\quad \text{on } \Gamma_2 \subset \partial\Omega, \tag{3b}$$

where $\boldsymbol{n}$ is the normal and tangential unit vectors on the boundaries Γ_1, Γ_2 of the open domain Ω; $\Gamma_1 \cup \Gamma_2 = \partial\Omega$, $\Gamma_1 \cap \Gamma_2 = \emptyset$.

2.2 Overview – CG and DG

The CG method (classical FEM) is a numerical method for solving (systems of) differential equations. It is based on *(i)* a computational domain discretized into cells of finite (not infinitesimal) size (finite elements), *(ii)* a variational formulation of the differential equation and *(iii)* a finite set of shape functions, each one being non-zero only on a small patch of mesh cells. The shape functions are usually chosen as piecewise polynomials that form a basis of a discrete space approximating the solution space, cf. Sect. 2.3. Being a linear combination of those shape functions, also the approximate solution is piecewise polynomial. An FEM is said to be *conforming* if the approximation it yields is continuous in every point.

The DG method generalizes the FEM in such a way that in general no continuity along the mesh cell edges is enforced. Thus, the approximate solution is piecewise polynomial, meaning polynomial on every single mesh cell. However, it may have jumps across the cell edges of the mesh. This jump resembles a non-zero *flux* from one mesh cell to the adjacent one given by the cell interface integrals. Describing and handling this flux is the main difference in the numerical scheme for a CG and a DG method.

2.3 Numerical scheme

In what follows we will derive a numerical approximation of (1)–(3). We will in particular concentrate on the derivation of the DG method, since the CG FEM is a standard method also in the framework of geophysical applications. Let $\Omega \subset \mathbf{R}^2$ be an open, bounded polygonal computational domain and $\mathcal{T}_h$ ($h > 0$ is a mesh parameter denoting the maximal edge length) denote a partition of the closure $\bar{\Omega}$ into a finite number of mesh elements. We denote a general mesh element by E and set $\mathcal{T}_h := \{E_i\}_{i \in I}$, where I is a suitable index set of all elements. We call two elements E_i, E_j neighbouring elements, if $E_i \cap E_j$ contains their common edge. We will only consider quadrilateral elements in this article, but results can be generalized also to the triangular case.

The approximate solution to our problem (1)–(3) is sought in the space of polynomial functions. We denote by $\mathrm{P}_k(E)$ the space of polynomials of (total) degree $\le k$ on a mesh element E and $\mathrm{Q}_k(E) = \mathrm{P}_{k,k}(E)$, where

$$\mathrm{P}_{k_1,k_2}(E) = \left\{ p(x_1, x_2) \mid p(x_1, x_2) = \sum_{\substack{i \le k_1 \\ j \le k_2}} a_{ij} x_1^i x_2^j \right\}.$$

Finite Element Basis Before introducing suitable discrete spaces X_h, Q_h which are used for the velocity and pressure discretization, we first present different finite element bases that are used in our numerical schemes. The elements listed below are, except for $\mathrm{Q}_1\mathrm{P}_0$, inf-sup stable, i.e., they fulfill the so-called LBB or inf-sup stability condition, see [57].

$\mathrm{Q}_1\mathrm{P}_0$ element: Although proven to be unstable [58] the seemingly easy-to-use $\mathrm{Q}_1\mathrm{P}_0$ element with bilinear velocity shape functions and piecewise constant pressure is still heavily applied in practice. Therefore, we will use it as a reference pointing out its benefits and limitations.

Raviart-Thomas element: For elliptic problems this element was introduced in 1977 [59]. We will consider only the lowest-order Raviart-Thomas element $\mathrm{RT}_0\mathrm{P}_0$. The velocity components can locally be written as $\mathrm{RT}_0(E) = \mathrm{P}_{1,0}(E) \times \mathrm{P}_{0,1}(E)$. Globally, the horizontal velocity component is piecewise linear and continuous in horizontal direction and piecewise constant and discontinuous in vertical direction. The vertical velocity component is the other way around, i.e., piecewise linear and continuous in vertical direction and piecewise constant and discontinuous in horizontal direction. The matching pressure space P_0 is piecewise constant and discontinuous.

As shown in [60] for the isoviscous case, the $\mathrm{RT}_0\mathrm{P}_0$ element in the corresponding numerical scheme resembles the finite difference (FD) staggered grid stencil. Raviart-Thomas elements of order k can, therefore, be considered a higher-order generalization of the FD method working on irregular meshes. Limitations to this consideration are given in section 3 for geodynamic benchmarks.
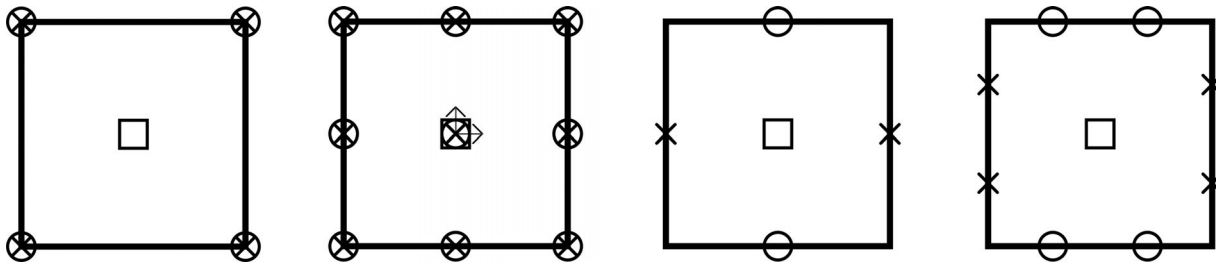
Fig. 1 Degrees of freedom (DOFs) for the elements Q_1P_0, Q_2P_1, lowest-order Raviart-Thomas RT_0P_0 and Brezzi-Douglas-Marini BDM_1P_0 (left to right). Crosses and circles denote DOFs for horizontal and vertical velocity, respectively. Squares and arrows denote pressure and pressure gradient DOFs.
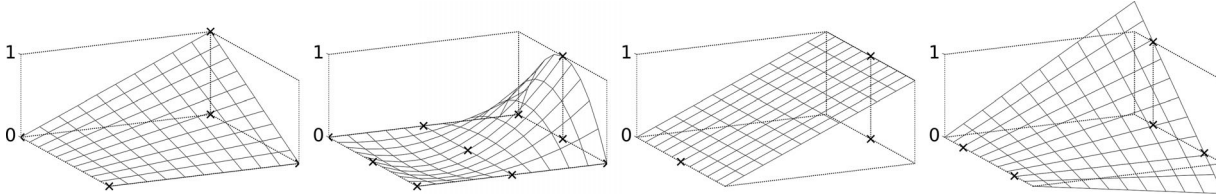

Fig. 2 Instances of basis functions for (horizontal) velocity component of the elements Q_1P_0, Q_2P_1, RT_0P_0, BDM_1P_0 (left to right).

Brezzi-Douglas-Marini element: This element was introduced in 1985 [61] following the Raviart-Thomas element in its approach to design a discrete basis of $H_0(\mathrm{div}, \Omega)$, cf. (4c), see also [62, §III.3]. Locally, it is bilinear like the Q_1P_0 element, $BDM_1(E) = Q_1(E)^2$ with $Q_1(E)$ defined above. Across mesh edges, it is continuous in normal direction and discontinuous in tangential direction like the RT_0P_0 element. The matching pressure space is piecewise constant and discontinuous.

Q_2P_1 element: This element is based on a biquadratic approximation for velocity and a piecewise linear approximation for pressure. On the same mesh this element reaches higher accuracy at increased computational cost compared to the Q_1P_0 element. As for the other elements the pressure approximation may encounter discontinuities across mesh edges. This element is commonly used for discretization of the Stokes flow.

In what follows we use the abbreviation Q_1P_0 or Q_2P_1 for the FEM based on using either the Q_1P_0 or the Q_2P_1 element, respectively. On the other hand we use the abbreviation RT_0P_0 or BDM_1P_0 for the DG method based on using either the RT_0P_0 or the BDM_1P_0 element, respectively.

Function Spaces   The finite element bases Q_1P_0 and Q_2P_1 yield well-known continuous finite element methods, see, e.g., [63, III.§6]. In what follows we define suitable discrete spaces X_h, Q_h for the discretization of velocity and pressure, respectively, that will be used in the framework of the discontinuous Galerkin scheme.

$$X_h = \{\boldsymbol{u} \in H_0(\mathrm{div}, \Omega) : \boldsymbol{u}|_E \in RT_0(E) \text{ or } BDM_1(E) \, \forall E, \, \boldsymbol{u} \cdot \boldsymbol{n} = 0 \text{ on } \partial\Omega\}, \tag{4a}$$

$$Q_h = \{q \in L^2(\Omega) : q|_E \in P_0(E) \, \forall E, \, \textstyle\int_\Omega q = 0\}, \tag{4b}$$

$$H_0(\mathrm{div}, \Omega) = \{\boldsymbol{u} \in (L^2(\Omega))^2 : \nabla \cdot \boldsymbol{u} \in L^2(\Omega), \boldsymbol{u} \cdot \boldsymbol{n} = 0 \text{ on } \partial\Omega\}. \tag{4c}$$

Thus, the approximation for the velocity is div-conforming, i.e. included in $H_0(\mathrm{div}, \Omega)$. It has continuous normal components across elements and will be globally divergence free in the space $H_0(\mathrm{div}, \Omega)$, cf. [60].

Scheme Derivation   We now introduce notations for the jump and average of a (scalar or vector-valued) quantity $\boldsymbol{u} \in \mathbf{R}^n$, $n \geq 1$, along an edge $e = E_i \cap E_j$ shared by two neighbouring mesh elements E_i, E_j with the respective outer normal vectors $\boldsymbol{n}_i$ pointing to E_j, and $\boldsymbol{n}_j$ pointing to E_i,

$$[\boldsymbol{u}]_{ij} := \boldsymbol{u}_j - \boldsymbol{u}_i, \qquad \langle \boldsymbol{u} \rangle_{ij} := \frac{\boldsymbol{u}_i + \boldsymbol{u}_j}{2}, \tag{5}$$

where $\boldsymbol{u}_i$ denotes the limiting value of $\boldsymbol{u}$ from the mesh elements E_i along edge e. The analogous notation holds for $\boldsymbol{u}_j$. Fixing either of the normal vectors $\boldsymbol{n}_i$, $\boldsymbol{n}_j$ as belonging to the edge e, we drop the index notation for the jump since $\boldsymbol{n}_i = -\boldsymbol{n}_j$ and thus $[\boldsymbol{u}]_{ij}\boldsymbol{n}_j = [\boldsymbol{u}]_{ji}\boldsymbol{n}_i =: [\boldsymbol{u}]\boldsymbol{n}_e$. Consequently, we fix either of the normal vectors on interior edges and refer to it as $\boldsymbol{n}_e$. For boundary edges $e \subset \partial\Omega$ the notation $\boldsymbol{n}_e$ refers to the unique outward pointing normal. Secondly, we note without proof the following Lemma, cf. e.g. [64],

Lemma 2.1. *For $\boldsymbol{a}, \boldsymbol{b} \in \mathbf{R}^n$, $n \geq 1$, (or $\boldsymbol{a} \in \mathbf{R}$, $\boldsymbol{b} \in \mathbf{R}^n$, $n > 1$) the following equality applies:*

$$[\boldsymbol{a} \cdot \boldsymbol{b}] = \langle \boldsymbol{a} \rangle \cdot [\boldsymbol{b}] + [\boldsymbol{a}] \cdot \langle \boldsymbol{b} \rangle. \tag{6}$$

Now, we will derive our DG approximation following [42], [65, 4.2 and 6.2], [66, 14.2]. Note that the different approach of [55] yields similar forms. First, multiplying the momentum conservation equation (1a) with a test function $\boldsymbol{\phi} \in X_h$ yields after elementwise integration by parts,

$$\int_E 2\mu \, \dot{\boldsymbol{\epsilon}}(\boldsymbol{\phi}) : \dot{\boldsymbol{\epsilon}}(\boldsymbol{v}) - \int_{\partial E} \boldsymbol{\phi} \cdot (\boldsymbol{\tau} \boldsymbol{n}_E) - \int_E p(\nabla \cdot \boldsymbol{\phi}) + \int_{\partial E} p\boldsymbol{\phi} \cdot \boldsymbol{n}_E = \int_E -\rho g \hat{\boldsymbol{z}} \cdot \boldsymbol{\phi}, \tag{7}$$

where $\boldsymbol{n}_E$ denotes the unit outer normal of the mesh cell E and $\boldsymbol{a} : \boldsymbol{b}$ the so-called Frobenius product, i.e., componentwise inner product of two matrices. Let us look in more details at the second term summed with respect to the mesh cells:

$$-\sum_{E \in \mathcal{T}_h} \int_{\partial E} \boldsymbol{\phi} \cdot (\boldsymbol{\tau} \boldsymbol{n}_E) = -\sum_{e \in \mathcal{F}_h} \int_e [\boldsymbol{\phi} \cdot \boldsymbol{\tau}] \, \boldsymbol{n}_e - \sum_{e \subset \partial \Omega} \int_e \boldsymbol{\phi} \cdot \boldsymbol{\tau} \boldsymbol{n}_e. \tag{8}$$

First, we would like to mention that the integrals along the boundary edges $e \subset \partial \Omega$ vanish due to the boundary conditions (3). Indeed, on Γ_2 the test function vanishes due to the Dirichlet boundary conditions. On Γ_1 we have $\sum_{e \subset \Gamma_1} \int_e \boldsymbol{\phi} \mu (\nabla \boldsymbol{v} + (\nabla \boldsymbol{v})^\top) \boldsymbol{n}_e = \sum_{e \subset \Gamma_1} \int_e \boldsymbol{\phi} \mu (\nabla \boldsymbol{v})^\top \boldsymbol{n}_e$, since $\nabla \boldsymbol{v} \cdot \boldsymbol{n}_e = \frac{\partial \boldsymbol{v}}{\partial \boldsymbol{n}_e} = 0$. Furthermore, we recall that Ω is a polygonal domain, thus on each boundary segment we have a constant outer normal. Applying both conditions from (3a) we finally obtain that $(\nabla \boldsymbol{v})^\top \boldsymbol{n}_e = (\sum_{j=1}^2 \frac{\partial v_j}{\partial x_1} n_{e,j}, \sum_{j=1}^2 \frac{\partial v_j}{\partial x_2} n_{e,j})^\top = \boldsymbol{0}$ on Γ_1.

Further, we exploit Lemma 2.1 and, as argued in [66], we apply the interior penalty method. Thus, we replace the normal flux term, $\boldsymbol{\tau} \boldsymbol{n}$, by the discrete flux, $\langle 2\tilde{\mu} \dot{\boldsymbol{\epsilon}}(\boldsymbol{v}) \rangle \boldsymbol{n}_e - \frac{\sigma}{|e|} [\boldsymbol{v}]$, where σ is a suitable positive weight parameter, cf. also, e.g., [42, 4.6], [60]. In our numerical experiments presented in Sect. 3 the parameter σ was chosen to be globally constant.

$$-\sum_{e \in \mathcal{F}_h} \int_e [\boldsymbol{\phi} \cdot \boldsymbol{\tau}] \, \boldsymbol{n}_e = -\sum_{e \in \mathcal{F}_h} \int_e [\boldsymbol{\phi}] \cdot \langle \boldsymbol{\tau} \rangle \, \boldsymbol{n}_e + \langle \boldsymbol{\phi} \rangle \cdot [\boldsymbol{\tau}] \, \boldsymbol{n}_e \tag{9}$$

$$= -\sum_{e \in \mathcal{F}_h} \int_e [\boldsymbol{\phi}] \cdot \boldsymbol{\tau} \boldsymbol{n}_e \tag{10}$$

$$\simeq -\sum_{e \in \mathcal{F}_h} \int_e [\boldsymbol{\phi}] \cdot \left(\langle 2\tilde{\mu} \dot{\boldsymbol{\epsilon}}(\boldsymbol{v}) \rangle \boldsymbol{n}_e - \frac{\sigma}{|e|} [\boldsymbol{v}] \right). \tag{11}$$

We have also used the fact that $\boldsymbol{\tau} \boldsymbol{n}_e$ is continuous across mesh edges for $\boldsymbol{v}$ being the exact solution, cf. [67]. Further, $\tilde{\mu}$ denotes an average viscosity value depending on the values of μ on the mesh cells that adhere to the respective edge e. We choose $\tilde{\mu}$ to be the geometric average accommodating the fact that μ may change by orders of magnitude. We note that, for the chosen benchmark setups, this yields smaller errors than taking the arithmetic or harmonic mean. For other ways of computing weighted averages in this context compare, e.g., [65, 4.5.2].

We note that the term $[\boldsymbol{v}] \cdot \langle 2\tilde{\mu} \dot{\boldsymbol{\epsilon}}(\boldsymbol{\phi}) \rangle$ is zero for $\boldsymbol{v}$ being the exact solution. Therefore, we could add it to (or subtract it from) the previous term without losing consistency. These considerations yield the following bilinear form a_h, which will be used for the numerical scheme,

$$a_h(\boldsymbol{v}, \boldsymbol{\phi}) = \sum_E \int_E 2\mu \dot{\boldsymbol{\epsilon}}(\boldsymbol{\phi}) : \dot{\boldsymbol{\epsilon}}(\boldsymbol{v}) + \sum_{e \in \mathcal{F}_h} \frac{\sigma}{|e|} \int_e [\boldsymbol{\phi}] \cdot [\boldsymbol{v}] \tag{12a}$$

$$-\sum_{e \in \mathcal{F}_h} \int_e [\boldsymbol{\phi}] \cdot \langle 2\mu \dot{\boldsymbol{\epsilon}}(\boldsymbol{v}) \rangle \boldsymbol{n}_e - \epsilon \sum_{e \in \mathcal{F}_h} \int_e [\boldsymbol{v}] \cdot \langle 2\mu \dot{\boldsymbol{\epsilon}}(\boldsymbol{\phi}) \rangle \boldsymbol{n}_e, \quad \boldsymbol{v}, \boldsymbol{\phi} \in X_h. \tag{12b}$$

For $\epsilon = 1, -1, 0$, this is refered to as the symmetric, nonsymmetric or incomplete interior penalty Galerkin method (SIPG, NIPG, IIPG), respectively. SIPG methods have been introduced in [64], NIPG in [68], IIPG in [69]. We refer also to other works, see, e.g., [52, 70–73] and the references therein, where full numerical analysis of the discontinous Galerkin method with SIP for the Laplace equation is available. For more details on the differences of these methods, we refer the reader to [74, 1.2], [65, 5.3] and the references therein. Numerical results presented in this paper were obtained using the NIPG ($\epsilon = -1$) that yielded best results for the considered benchmark problems.

The weak form of the incompressibility condition (1b) yields the bilinear form b_h and is given by:

$$0 = b_h(\boldsymbol{v}, q) = \sum_E \int_E (\nabla \cdot \boldsymbol{v}) q, \quad q \in Q_h. \tag{13}$$

To discretize the pressure terms from the momentum equation we extend the bilinear form b_h, cf. [65, 6.1],

$$b_h^*(\boldsymbol{\phi}, p) = -b_h(\boldsymbol{\phi}, p) + \sum_{e \in \mathcal{F}_h} \int_e [p] \, \boldsymbol{\phi} \cdot \boldsymbol{n}_e + \sum_{e \subset \partial \Omega} \int_e p\boldsymbol{\phi} \cdot \boldsymbol{n}_e, \tag{14}$$

where we used that $\boldsymbol{\phi} \cdot \boldsymbol{n}_e$ is continuous across mesh edges. Note again that the boundary integrals vanish due to Eq. (3).

Now, we can state our DG approximation scheme: Find $(v, p) \in X_h \times Q_h$ such that

$$a_h(v, \phi) + b_h^*(\phi, p) = \int_\Omega -\rho g \hat{z} \cdot \phi, \quad \forall \phi \in X_h, \tag{15a}$$

$$b_h(v, q) = 0, \quad \forall q \in Q_h. \tag{15b}$$

In [55] analytic properties of a large class of divergence-free DG methods have been investigated. The authors studied div-conforming spaces, which satisfy the condition $\nabla \cdot X(E) \subseteq P(E)$, where $X(E)$ and $P(E)$ are local spaces for the approximation of velocity and pressure, respectively. Note that our local element RT_0P_0 satisfies the above condition. The use of the local space BDM_{k+1}/P_k for velocity and pressure, respectively, have been analyzed in [75] in the framework of DG FEM. For a large class of DG methods (including our particular choice (15)) the stability and accuracy have been investigated theoretically in [55]. In particular, it has been proven that the resulting methods satisfy the inf-sup stability condition and that the following error estimates hold.

Let us denote by v, p, v_h, p_h the exact and approximate solutions (velocity vector and pressure), respectively. Moreover let $v \in H^{k+1}(\Omega)$, $p \in H^k(\Omega)$ is a regular solution and $\| \cdot \|_{1,h}$ is a suitable discrete H^1 norm in the broken Sobolev space X_h, i.e., $\|u_h\|_{1,h}^2 = \sum_E \int_E (\nabla u_h)^2 \mathrm{d}x + \sum_e \int_e \frac{\sigma}{h} |[u_h]|^2$ for any $u_h \in X_h$. Then it holds

$$\|v - v_h\|_{1,h} + \|p - p_h\|_{L^2(\Omega)} \le c h^k (\|v\|_{k+1} + \|p\|_k), \tag{16}$$

where $k \ge 1$, $c > 0$ is a constant independent of the mesh size h. Moreover, the approximate velocity v_h is exactly divergence-free and the resulting DG methods are conservative, energy-stable and optimally convergent, cf. [55] and [75].

Let us also point out that in [60] the author investigates the use of the RT_0P_0 element in the framework of divergence-free DG methods. It has been proven that such a DG scheme is algebraically equivalent to the standard MAC finite difference scheme, that is often used in engineering applications in order to approximate the Stokes problem. Using this fact, we can apply the recent result of Li and Sun [76] who have proven superconvergence of the MAC scheme, i.e., the discrete L^2 errors of pressure, velocity as well as gradient of velocity are of second order.

In this paper we compare the behaviour of the above DG methods and standard, i.e. continuous finite elements, for some typical geophysical tests. Recall that when we apply CG-FEM method the space X_h is a discrete space approximating $(H^1(\Omega))^2$ with cellwise bilinear Q_1 or cellwise biquadratic functions Q_2. For the latter the pressure space Q_h is the space of cellwise *linear* functions with mean value zero. Thus, we do not require that the discrete velocities for CG-FEM are div-conforming (i.e., in $H_0(\mathrm{div}, \Omega)$). Note that using the same bilinear forms without edge integrals the formulation above coincides with the standard variational formulation of incompressible Stokes flow in a CG-FEM setting, see, e.g., [63, III.§6], [66, 12.2].

2.4 Benchmark setups

SolCx Benchmark   The analytic solution to this benchmark was derived by Zhong [77] and our implementation follows [22]. We include a Matlab function (SolCx.m) to compute the analytic solution in the online supplement to this article that is based on the one provided in Underworld [33]. The setup resembles a simplified mantle convection model with a lateral viscosity jump caused by, e.g., a material interface. The flow is driven by a prescribed smooth density field.

Rayleigh-Taylor Instability   This fluid-interface benchmark is used to test the velocity solution of gravity driven flows, see [12,35,78]. The boundary between the two fluids is perturbed by a sinusoidal perturbation of low, yet finite, amplitude A. By stretching the domain horizontally while keeping the relative shape of the perturbation we change its wavelength. This variation affects the maximal values for the vertical velocity at the interface. The analytic velocity solution is obtained for an infinitesimal amplitude and derived in detail in [78]. It is computed in a separate Matlab function (diapGrwth.m) in the online supplement to this article.

3   Numerical experiments

In this section we describe the methodology for comparison of methods and discretizations for the above benchmarks and how to quantify computational costs of the different discretizations. All simulations using the RT_0P_0 element were done with $\sigma = 1$ while for all simulations using the BDM_1P_0 element σ was set to $\sigma = \frac{1}{h}$, where h denotes the edge length. This choice yielded the best results.

Note that the system was solved directly and that we did not investigate the performance of the method in larger scale simulations.
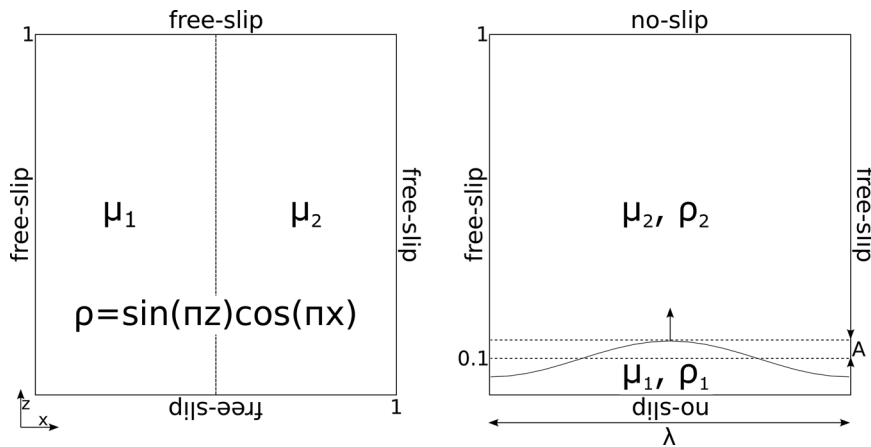
Fig. 3 Benchmark setups SolCx (left) and Rayleigh-Taylor instability (right) with material viscosities μ_1, μ_2 and densities ρ (SolCx setup), ρ_1, ρ_2 (Rayleigh-Taylor).

3.1 SolCx benchmark

The flow in the SolCx Benchmark is driven by a prescribed density field $\rho = -\sin(\pi z)\cos(\pi x)$ in the open domain $\Omega = (0, 1) \times (0, 1)$, the gravity $g = 1$ is normalized. The flow is subjected to free-slip boundary conditions as given in (3a), see Fig. 3 (left).

We consider two test cases: an isoviscous setup ($\mu_1 = \mu_2 = 1$) and a setup with a lateral viscosity jump of three orders of magnitude ($\mu_1 = 1$, $\mu_2 = 10^3$) at $x = .5$. For both cases, we computed the discrete L^2 error for velocity and for pressure as well as the H^1 error for velocity with numerical quadratures of sufficient order. Having obtained errors on consecutively refined meshes we can determine the order of convergence for pressure and velocity. Note that we only considered cases where element edges are aligned with the viscosity jump. Strong variations in the viscosity within elements leads to reduced order of convergence, cf. [18, 19].

Isoviscous Setup For the discretizations where the velocity is approximated with (bi-)linear basis functions (RT_0P_0, Q_1P_0, BDM_1P_0) we obtain second order convergence for the velocity measured in L^2 and H^1 norms. The L^2 error obtained with the RT_0P_0 element is slightly smaller than for Q_1P_0 and BDM_1P_0. Apparently, the RT_0P_0 element shows the superconvergence behavior mentioned in Sect. 2.3, cf. [76]. The Q_1P_0 and BDM_1P_0 elements are on the same level. The higher order of the Q_2P_1 element yields fourth order convergence for the velocity measured in the L^2 norm. As the cross derivatives $\partial_x \boldsymbol{v}_z$, $\partial_z \boldsymbol{v}_x$ vanish locally for the RT_0P_0 element, it does not converge with respect to the H^1 norm and, hence, its plot is omitted. The other three elements yield H^1 errors on about the same level (BDM_1P_0 smallest, Q_2P_1 largest).

The L^2 pressure error differs only slightly for the RT_0P_0 and the Q_2P_1 element as well as for the Q_1P_0 and the BDM_1P_0 element. For the latter ones it is at least two orders of magnitude smaller and has higher rate of convergence, which seems to be influenced by superconvergence effects for this particular setup.

Let us consider the errors with respect to the number of degrees of freedom (DOFs) needed to reach a certain accuracy. The Q_2P_1 element still yields the smallest velocity error in the L^2 norm. On the other hand, the Q_1P_0 element performs slightly better than the BDM_1P_0 element (and a lot better than the Q_2P_1 element) in terms of the H^1 error in the velocity and the pressure error.

For the velocity and pressure error in the isoviscous SolCx setup see Figs. 5 and 6.

Lateral Viscosity Jump In this setup the velocity errors show a similar behavior as for the isoviscous case, i.e., the BDM_1P_0 and Q_1P_0 element converge with second order to the analytic solution with the error being at the same order of magnitude, while the Q_2P_1 element converges with fourth order and, therefore, reaches much higher accuracy at the same resolution. For the BDM_1P_0 element the convergence order measured in the H^1 norm is only 1.3, approximately, while the two conforming elements keep the order 2. The pressure errors for these three elements are of similar order and converge with second order.

Considering the number of degrees of freedom the elements' performance is similar to the isoviscous case. The Q_2P_1 element yields the best L^2 error for the velocity while the Q_1P_0 element yields highest accuracy in terms of the H^1 error for the velocity and L^2 error for the pressure. For the velocity and pressure error in the SolCx setup with discontinuous viscosity see Figs. 7 and 8.

We omit the RT_0P_0 element for this setup as it does not converge to the analytic solution. Due to the simple structure of this element no coupling of the two velocity components can be captured in the numerical scheme given in section 2.3. As the cross derivatives $\partial_x \boldsymbol{v}_z$, $\partial_z \boldsymbol{v}_x$ vanish element-wise, shear stress components are not taken into account in the discrete
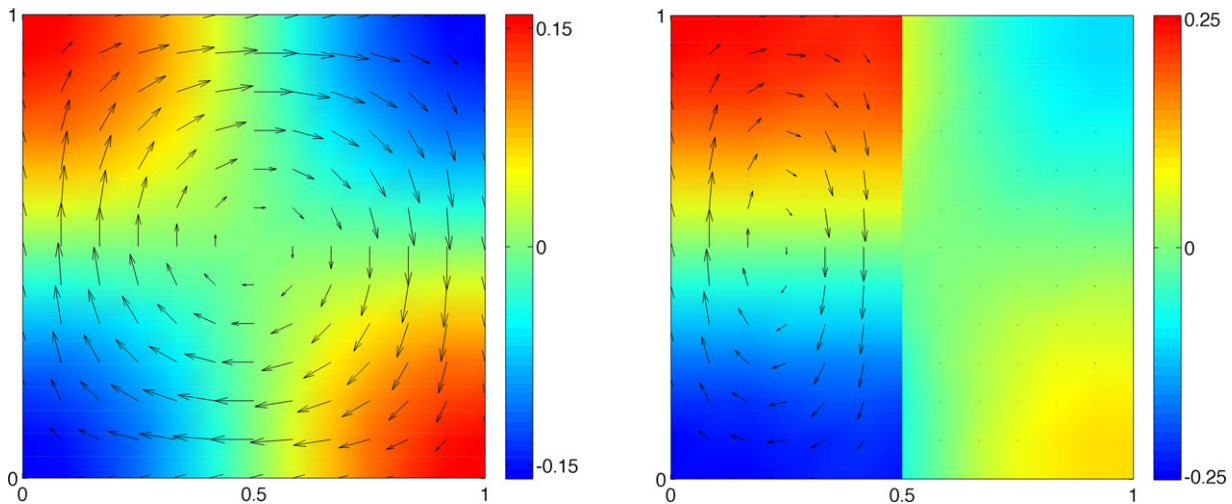
Fig. 4 Analytic solution in SolCx benchmark as given by [77] for velocity (arrows) and pressure (color-coded). Left: Isoviscous setup, $\mu_1 = \mu_2 = 1$. Right: Viscosity jump of three orders of magnitude, $\mu_1 = 1$, $\mu_2 = 10^3$. The reference arrow lengths are 2.53×10^{-2} and 3.60×10^{-3}, respectively, for the arrow originating at the point $(x = 0, z = .5)$. Note that the pressure is discontinuous in the variable viscosity setup and the jump is aligned with the viscosity jump. The analytic solution for the isoviscous setup is $\boldsymbol{v} = [-\sin(\pi x)\cos(\pi z); \cos(\pi x)\sin(\pi z)]/4\pi^2$, $p = -\cos(\pi x)\cos(\pi z)/2\pi$. The analytic solution of the variable-viscosity setup can be found in [77].
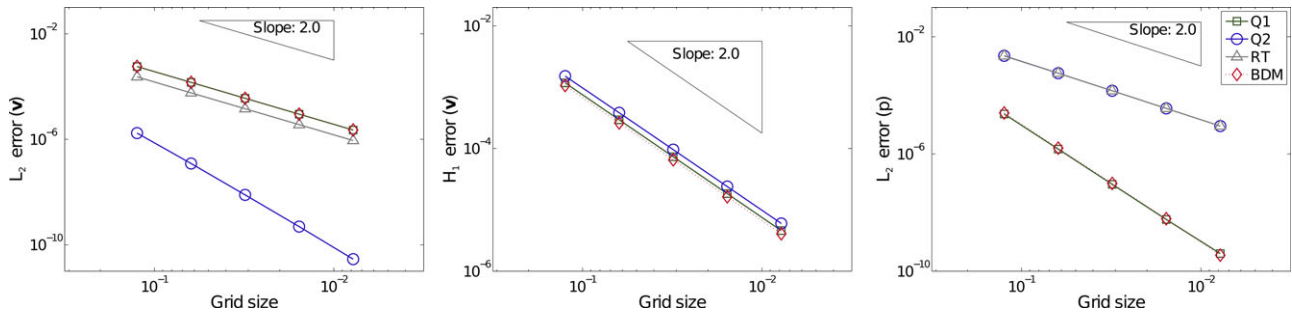
Fig. 5 Isoviscous SolCx Benchmark: L^2 (left) and H^1 (center) errors for velocity and L^2 error for pressure (right) for the four discretizations Q_1P_0, Q_2P_1, RT_0P_0 and BDM_1P_0. The slope of the plots corresponds to the order of convergence towards the analytic solution when increasing the mesh resolution, i.e., decreasing the grid size.
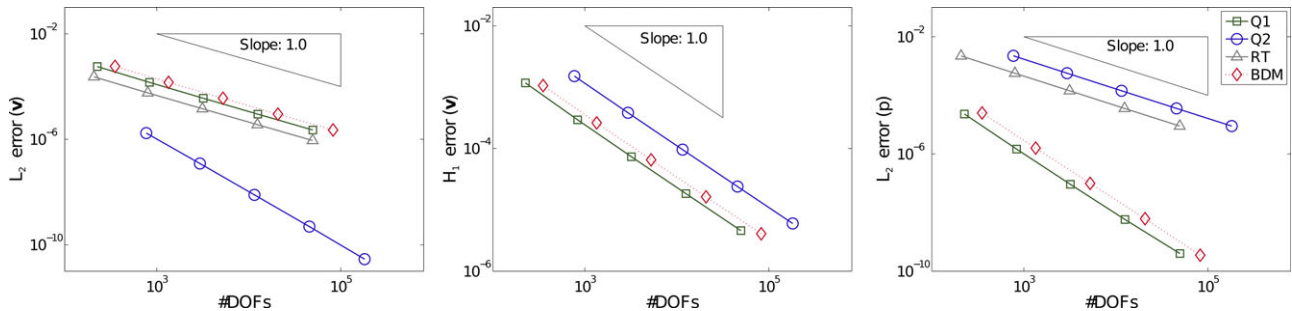

Fig. 6 Isoviscous SolCx Benchmark: L^2 (left) and H^1 (center) errors for velocity and L^2 error for pressure (right) for the four discretizations Q_1P_0, Q_2P_1, RT_0P_0 and BDM_1P_0. The slope of the plots corresponds to the order of convergence towards the analytic solution when increasing the number of degrees of freedom.

scheme. Shear stress is zero in the isoviscous SolCx setup but non-zero for discontinuous viscosity. This explains why the RT_0P_0 element converges in the isoviscous case but not in the discontinuous viscosity case. We aim to further investigate this problem in a future study.

We can deduce from Figs. 5 and 7 that the BDM_1P_0 element has about the same accuracy (in terms of the L^2 errors) as the Q_1P_0 element for any fixed resolution. This is to be expected as both elements are of the same order, i.e. velocity
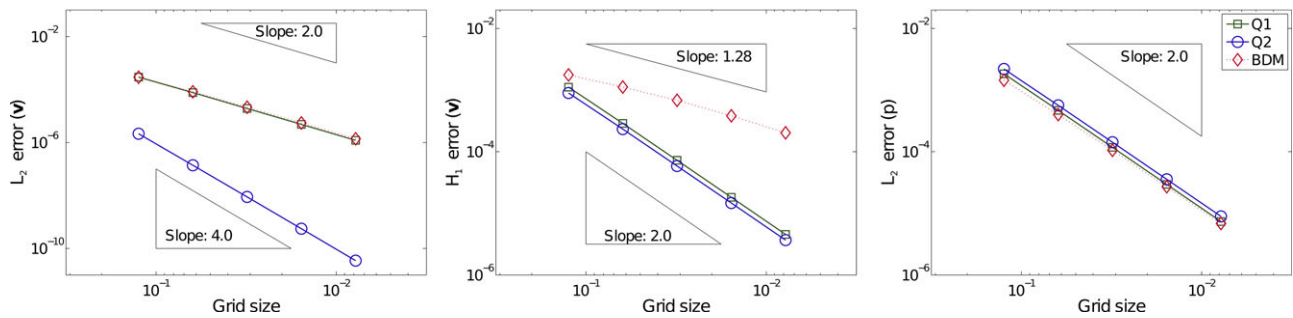
Fig. 7 Variable Viscosity SolCx Benchmark: L^2 (left) and H^1 (center) errors for velocity and L^2 error for pressure (right) for the three discretizations Q_1P_0, Q_2P_1 and BDM_1P_0. The slope of the plots corresponds to the order of convergence towards the analytic solution when increasing the mesh resolution, i.e., decreasing the grid size.
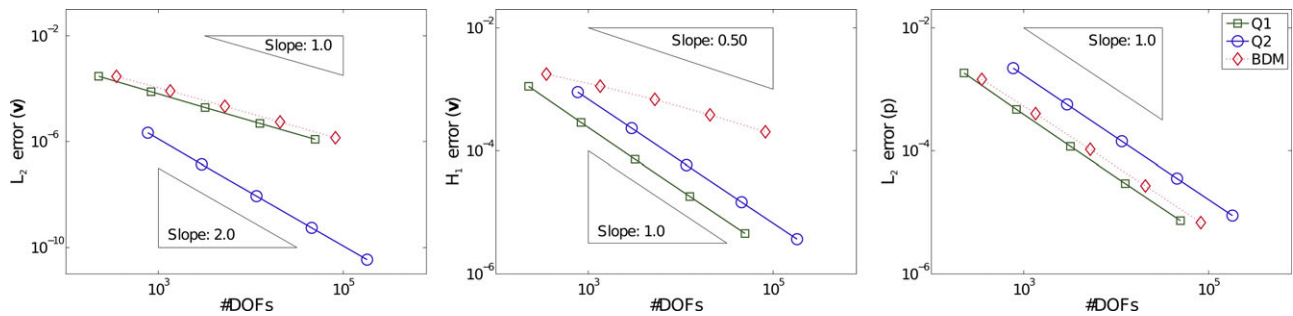

Fig. 8 Variable Viscosity SolCx Benchmark: L^2 (left) and H^1 (center) errors for velocity and L^2 error for pressure (right) for the three discretizations Q_1P_0, Q_2P_1 and BDM_1P_0. The slope of the plots corresponds to the order of convergence towards the analytic solution when increasing the number of degrees of freedom.

is approximated with piecewise bilinear, pressure is approximated with piecewise constant shape functions. The RT_0P_0 element is computationally cheaper, yielding similar accuracy in simple setups like the isoviscous SolCx setup but fails for setups with non-zero shear stress. The Q_2P_1 element, being of higher order, yields higher accuracy and higher order of convergence at the price of increased computational costs.

While the Q_1P_0 and Q_2P_1 element keep the L^2 order of convergence for the velocity when changing to the H^1 norm, the convergence order of the BDM_1P_0 element decreases.

3.2 Rayleigh-Taylor instability

In the Rayleigh-Taylor instability benchmark the flow is driven by the density difference $\Delta\rho = \rho_2 - \rho_1$ of the two material layers. Both, the density difference $\Delta\rho = 1$ and the gravity $g = 1$ are normalized. The computational domain is set to be $\Omega = (0, \lambda) \times (0, z_{max})$, where $z_{max} = 1$, see Fig. 3 (right). The material interface follows a mesh edge with a sinusoidal perturbation of amplitude A and wavelength λ, i.e., the elements adjacent to the perturbed edge are slightly deformed. Hence, the mesh is *not* globally regular anymore. We vary the viscosity contrast $10^{-3} \leq \mu_2/\mu_1 \leq 10^3$ and study the vertical velocity v_z at the tip of the sinusoidal perturbation. The magnitude of this velocity also depends on the wavelength λ, i.e., for every viscosity contrast there is one dominant wavelength λ^* that yields a maximal magnitude for the vertical velocity in this location. We vary the wavelength λ in a certain range around the dominant wavelength λ^*_{exp} that we determined experimentally, see the axis labels in Fig. 9 for the ranges of $\varphi = 2\pi(z_{max} - z_{jump})/\lambda$, $z_{max} = 1$, $z_{jump} = 0.1$.

In this setup, the free-slip condition is imposed at the vertical boundaries, no-slip at the horizontal boundaries, see (3). We run two sets of experiments. Firstly, we fix the resolution to 50 by 50 elements. Secondly, we choose the resolution such that for all elements it yields approximately the same number of non-zero entries in the system matrix. In both cases we compute the maximum vertical velocity v_z for different wavelengths λ of the sinusoidal perturbation by changing the width of the domain and we vary the viscosity contrasts between 10^{-3} and 10^3, fixing the perturbation amplitude at $A = 10^{-4}$. A non-dimensional growth factor $K_{an} = \frac{v_z}{A}\frac{2\mu_2}{\Delta\rho\,z_{jump}g}$ can be analytically derived as given in [78, sec. 6] and [12, sec. 16.2]. We compare the numerically retrieved value of K to the analytic one. For the same reasons as in the previous section we omit the RT_0P_0 element here.
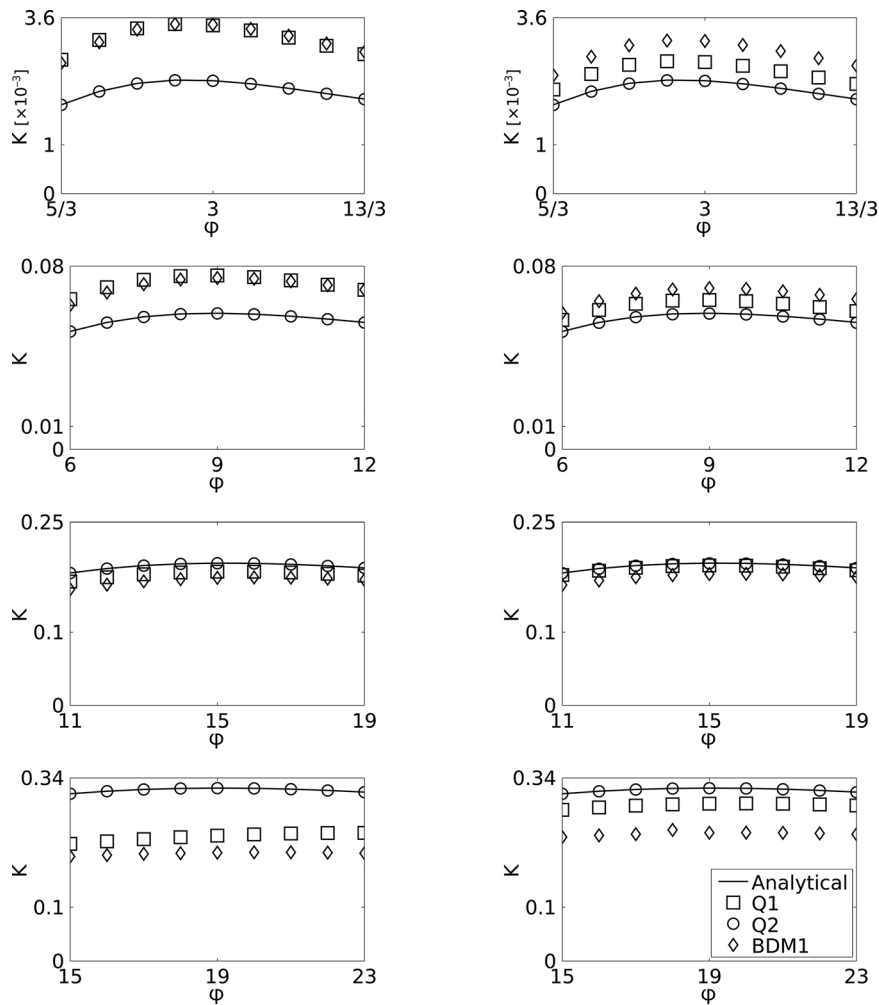
Fig. 9 Rayleigh-Taylor Instability Benchmark: Non-dimensional growth factor K versus frequency $\varphi = 2\pi (z_{max} - z_{jump})/\lambda$, $z_{max} = 1$, $z_{jump} = .1$. Solid lines give the analytically obtained value K_{an} at the tip of the sinusoidal perturbation (i.e., where vertical velocity is maximal). Top to bottom: Viscosity contrasts $\mu_2/\mu_1 = 10^3, 10^1, 10^0, 10^{-3}$. Left: Errors for Q_1P_0, Q_2P_1, BDM_1P_0 at fixed mesh resolution of 50 by 50. Right: Errors for Q_1P_0 (mesh resolution 90 by 90), Q_2P_1 (40 by 40), BDM_1P_0 (60 by 60), i.e., such that the system matrix has approximately 4.5×10^5 non-zero entries.

We shall first consider the case $\mu_2/\mu_1 \leq 1$, i.e., the top layer viscosity being less or equal to the bottom layer viscosity, with fixed resolution of 50 by 50 elements, see Fig. 9, bottom left. The Q_2P_1 element, as in all other cases, very accurately resembles the analytic value of the maximum vertical velocity while the Q_1P_0 and the BDM_1P_0 elements deviate stronger, see Tab. 1. Yet, the relative errors for the latter two stay in the same range.

For the same viscosity contrasts, but roughly equivalent memory usage of all three elements (Fig. 9, bottom right), the Q_2P_1 element is still the best choice. The relative error for the Q_1P_0 element is less than half of the error for the BDM_1P_0 element, see Tab. 2.

In the case $\mu_2/\mu_1 > 1$, i.e. the top layer being more viscous than the bottom layer, the BDM_1P_0 element yields a better approximation to the maximum vertical velocity than the Q_1P_0 element. Still, the Q_2P_1 element gives much higher accuracy, see Fig. 9, top left, and Tab. 1. For equivalent memory usage (Fig. 9, top right, Tab. 2), this behavior changes partially. For some wavelengths at viscosity contrast $\mu_2/\mu_1 = 10^3$ the BDM_1P_0 element yields a smaller error, for others the Q_1P_0 element does. For $\mu_2/\mu_1 = 10^1$ the Q_1P_0 error, all in all, is smaller than the error obtained with the BDM_1P_0 element.

Similar to the SolCx benchmark, using the Q_2P_1 element in the Rayleigh-Taylor instability benchmark, see Fig. 9, we obtain very accurate approximations for any considered viscosity contrast. On the one hand, we can see the BDM_1P_0 and Q_1P_0 elements yielding an error of equal order of magnitude for the bottom layer viscosity being greater or equal to the top layer viscosity ($\mu_1 \geq \mu_2$). On the other hand, when the top layer viscosity exceeds the bottom layer viscosity, the BDM_1P_0 element yields better results than the Q_1P_0 element.

Table 1 Relative errors $e_{\mathrm{rel}} = \left| \frac{K - K_{\mathrm{an}}}{K_{\mathrm{an}}} \right|$ for the three elements at $\varphi(\lambda^*_{\mathrm{exp}})$ in the middle of the chosen range. Resolution for all elements fixed at 50 by 50 elements.

μ_2/μ_1	Q_1P_0	$e_{\mathrm{rel}}(\lambda^*_{\mathrm{exp}})$ Q_2P_1	BDM_1P_0
10^3	4.9×10^{-1}	1.5×10^{-3}	5.0×10^{-1}
10^1	2.8×10^{-1}	1.4×10^{-3}	2.6×10^{-1}
10^0	6.0×10^{-2}	8.4×10^{-4}	1.0×10^{-1}
10^{-3}	2.7×10^{-1}	3.6×10^{-4}	3.7×10^{-1}

Table 2 Relative errors $e_{\mathrm{rel}} = \left| \frac{K - K_{\mathrm{an}}}{K_{\mathrm{an}}} \right|$ for the three elements at $\varphi(\lambda^*_{\mathrm{exp}})$ in the middle of the chosen range. Resolution for Q_1P_0, Q_2P_1, BDM_1P_0 element is 90 by 90, 40 by 40, 60 by 60 elements, respectively, yielding approximately the same memory usage for all three elements ($\approx 4.5 \times 10^5$ non-zero entries in system matrix).

μ_2/μ_1	Q_1P_0	$e_{\mathrm{rel}}(\lambda^*_{\mathrm{exp}})$ Q_2P_1	BDM_1P_0
10^3	1.6×10^{-1}	2.4×10^{-3}	3.5×10^{-1}
10^1	9.7×10^{-2}	2.5×10^{-3}	1.8×10^{-1}
10^0	1.6×10^{-2}	1.6×10^{-3}	7.7×10^{-2}
10^{-3}	9.0×10^{-2}	7.5×10^{-4}	2.6×10^{-1}

Table 3 Number of global degrees of freedom (DOFs) and of non-zero entries (NNZs) in the system matrix on a square 32-by-32-mesh for the four discretizations. Note that the Q_1P_0 and Q_2P_1 elements are used in the standard finite element framework while the RT_0P_0 and the BDM_1P_0 elements are used in the DG scheme derived in Sect. 2.3.

Element	DOFs	NNZs
RT_0P_0	3136	2.6×10^4
Q_1P_0	3202	4.8×10^4
BDM_1P_0	5248	1.2×10^5
Q_2P_1	11 522	3.1×10^5

3.3 Computational costs

Finally, we list the number of entries in the system matrix for the different discretizations as an indicator for computational costs of the solution and how much memory its assembly requires, see Tab. 3. It can be observed that the RT_0P_0 element is the cheapest one considered here. However, its drawbacks are obvious, as it fails to converge in relevant variable viscosity benchmark setups.

If one considers memory usage instead of mesh resolution one obtains different observations. For a fixed memory the Q_1P_0 element gives a higher accuracy than the BDM_1P_0 element that seemed to be competitive when fixing the mesh resolution, cf. Figs. 6, 8.

In any case, regarding fixed memory limitations or fixed resolution, the Q_2P_1 element has best over-all performance.

4 Conclusions

The main aim of this paper was to study behaviour of the DG finite element method based on the use of div-conforming elements to approximate the Stokes flow with variable viscosity and examine how it compares in terms of accuracy and memory usage to the standard CG finite element method for some typical geodynamic benchmark setups. In the DG scheme we employ the Raviart-Thomas (RT_0P_0) and the Brezzi-Douglas-Marini element (BDM_1P_0). In contrast to the Q_1P_0 finite element they fulfill the LBB stability condition, implying that they are more reliable.

We showed that the overall results are as accurate or more accurate than the ones obtained with the Q_1P_0 element in a standard finite element scheme considering a fixed mesh resolution. Yet, the Q_1P_0 CG method yields better results than the DG method using the BDM_1P_0 element when considering a fixed memory limitation. Secondly, being of first order both of them are computationally less expensive than the Q_2P_1 element. However, whenever a second-order FEM like Q_2P_1 is computationally feasible, higher accuracy can be obtained compared to the DG method based on the BDM_1P_0 element or the Q_1P_0 element in the classical FEM scheme.

The divergence-conforming property of the BDM_1P_0 and the RT_0P_0 element has been seen to be advantageous for, e.g., Navier-Stokes equations [55] or Darcy flow [56]. However, in the tested benchmark setups this does not produce noticable benefits. We would like to investigate this point in our future study on different test cases.

The BDM_1P_0 element yields good results in all tested setups and offers an alternative to the LBB-unstable Q_1P_0 element. The setups presented in this article do not lead to common instabilities of the Q_1P_0 element. However, we want to point out that for the Stokes flow the reliability of the BDM_1P_0 element is its major advantage when being compared to the Q_1P_0 element. This could well be taken as justification to deploy this discretization.

Due to the flexibility of *hp*-refinement within the DG methods, it is possible to apply low order discretizations in the vicinity of viscosity jumps, but higher order polynomials in the areas with constant or smoothly varying viscosity. This might be a promising future direction for complex geodynamic simulations.

References

[1] P. A. Allen and J. R. Allen, Basin Analysis: Principles and Applications (Wiley, 2005).

[2] C. J. Warren, C. Beaumont, and R. A. Jamieson, Modelling tectonic styles and ultra-high pressure (UHP) rock exhumation during the transition from oceanic subduction to continental collision, Earth Planet. Sc. Lett. **267**(1–2), 129–145 (2008).

[3] B. J. P. Kaus, C. Steedman, and T. W. Becker, From passive continental margin to mountain belt: Insights from analytical and numerical models and application to Taiwan, Phys. Earth Planet. Inter. **171**(1–4), 235–251 (2008).

[4] S. M. Lechmann, S. M. Schmalholz, G. Hetényi, D. A. May, and B. J. P. Kaus, Quantifying the impact of mechanical layering and underthrusting on the dynamics of the modern India-Asia collisional system with 3-D numerical models, J. Geophys. Res. **119**(1), 616–644 (2014).

[5] L. Moresi, P. G. Betts, M. S. Miller, and R. A. Cayley, Dynamics of continental accretion, Nature (Advance online publication) (2014).

[6] F. Crameri, H. Schmeling, G. J. Golabek, T. Duretz, R. Orendt, S. J. H. Buiter, D. A. May, B. J. P. Kaus, T. V. Gerya, and P. J. Tackley, A comparison of numerical surface topography calculations in geodynamic modelling: An evaluation of the 'sticky air' method, Geophys. J. Int. **189**(1), 38–54 (2012).

[7] G. Schubert, D. L. Turcotte, and P. Olson, Mantle Convection in the Earth and Planets (Cambridge University Press, 2001).

[8] Y. Deubelbeiss, B. J. P. Kaus, J. A. D. Connolly, and L. Caricchi, Potential causes for the non-Newtonian rheology of crystal-bearing magmas, Geochem. Geophy. Geosy. **12**(5) (2011).

[9] T. Keller, D. A. May, and B. J. P. Kaus, Numerical modelling of magma dynamics coupled to tectonic deformation of lithosphere and crust, Geophys. J. Int. **195**(3), 1406–1442 (2013).

[10] T. E. Johnson, M. Brown, B. J. P. Kaus, and J. A. van Tongeren, Delamination and recycling of Archaean crust caused by gravitational instabilities, Nature Geosci. **7**(1), 47–52 (2014).

[11] D. L. Turcotte and G. Schubert, Geodynamics (Cambridge University Press, 2002).

[12] T. V. Gerya, Introduction to Numerical Geodynamic Modelling (Cambridge University Press, 2010).

[13] A. Ismail-Zadeh and P. Tackley, Computational Methods for Geodynamics (Cambridge University Press, 2010).

[14] T. W. Becker and B. J. P. Kaus, Numerical Geodynamics – An introduction to computational methods with focus on solid Earth applications of continuum mechanics, http://geodynamics.usc.edu/%7Ebecker/preprints/Geodynamics540.pdf (Lecture Notes), 2010.

[15] B. J. P. Kaus, H. Mühlhaus, and D. A. May, A stabilization algorithm for geodynamic numerical simulations with a free surface, Physics of the Earth and Planetary Interiors **181**(1–2), 12–20 (2010).

[16] P. J. Tackley, Modelling compressible mantle convection with large viscosity contrasts in a three-dimensional spherical shell using the yin-yang grid, Phys. Earth Planet. Inter. **171**(1–4), 7–18 (2008).

[17] M. Thielmann and B. J. P. Kaus, Shear heating induced lithospheric-scale localization: Does it result in subduction?, Earth Planet. Sc. Lett. **359–360**, 1–13 (2012).

[18] Y. Deubelbeiss and B. J. P. Kaus, Comparison of Eulerian and Lagrangian numerical techniques for the Stokes equations in the presence of strongly varying viscosity, Phys. Earth Planet. Inter. **171**(1–4), 92–111 (2008).

[19] M. Thielmann, D. May, and B. Kaus, Discretization errors in the hybrid finite element particle-in-cell method, Pure Appl. Geophys. **171**(9), 2165–2184 (2014).

[20] P. J. Tackley, Effects of strongly temperature-dependent viscosity on time-dependent, three-dimensional models of mantle convection, Geophys. Res. Lett. **20**(20), 2187–2190 (1993).

[21] T. V. Gerya and D. A. Yuen, Characteristics-based marker-in-cell method with conservative finite-differences schemes for modeling geological flows with strongly variable transport properties, Phys. Earth Planet. Inter. **140**(4), 293–318 (2003).

[22] D. A. May and L. Moresi, Preconditioned iterative methods for stokes flow problems arising in computational geodynamics, Phys. Earth Planet. Inter. **171**(1–4), 33–47 (2008).

[23] T. Duretz, D. A. May, T. V. Gerya, and P. J. Tackley, Discretization errors and free surface stabilization in the finite difference and marker-in-cell method for applied geodynamics: A numerical study, Geochem. Geophy. Geosy. **12**(7), 1200–1225 (2011).

[24] C. Hüttig and K. Stemmer, Finite volume discretization for dynamic viscosities on Voronoi grids, Phys. Earth Planet. Inter. **171**(1–4), 137–146 (2008).

[25] S. A. Melchior, V. Legat, P. v. Dooren, and A. J. Wathen, Analysis of preconditioned iterative solvers for incompressible flow problems, Int. J. Numer. Meth. Fluids **68**(3), 269–286 (2012).

[26] M. Benzi, G. H. Golub, and J. Liesen, Numerical solution of saddle point problems, Acta numerica **14**, 1–137 (2005).

[27] C. Burstedde, O. Ghattas, M. Gurnis, G. Stadler, E. Tan, T. Tu, L. C. Wilcox, and S. Zhong, Scalable adaptive mantle convection simulation on petascale supercomputers, in: Proceedings of the 2008 ACM/IEEE Conference on Supercomputing, SC '08 (IEEE Press, Piscataway, NJ, USA, 2008), pp. 62:1–62:15.

[28] C. Burstedde, G. Stadler, L. Alisic, L. C. Wilcox, E. Tan, M. Gurnis, and O. Ghattas, Large-scale adaptive mantle convection simulation, Geophys. J. Int. **192**(3), 889–906 (2013).

[29] M. Furuichi, D. A. May, and P. J. Tackley, Development of a Stokes flow solver robust to large viscosity jumps using a Schur complement approach with mixed precision arithmetic, J. Comput. Phys. **230**(24), 8835–8851 (2011).

[30] B. E. Griffith, An accurate and efficient method for the incompressible Navier-Stokes equations using the projection method as a preconditioner, J. Comput. Phys. **228**(20), 7565–7595 (2009).

[31] M. Cai, A. J. Nonaka, J. B. Bell, B. E. Griffith, and A. Donev, Efficient Variable-Coefficient Finite-Volume Stokes Solvers, arXiv preprint arXiv:1308.4605v2 (2013).

[32] S. Zhong, Constraints on thermochemical convection of the mantle from plume heat flux, plume excess temperature, and upper mantle temperature, J. Geophys. Res. **111**(B4) (2006).

[33] L. Moresi, S. Quenette, V. Lemiale, C. Mériaux, B. Appelbe, and H. B. Mühlhaus, Computational approaches to studying non-linear dynamics of the crust and mantle, Phys. Earth Planet. Inter. **163**(1–4), 69–82 (2007).

[34] M. Dabrowski, M. Krotkiewski, and D. W. Schmid, MILAMIN: MATLAB-based finite element method solver for large problems, Geochem. Geophy. Geosy. **9**(4) (2008).

[35] A. A. Popov and S. V. Sobolev, SLIM3D: A Tool for Three-dimensional Thermomechanical Modeling of Lithospheric Deformation with Elasto-visco-plastic Rheology, Phys. Earth Planet. Inter. **171**(1–4), 55–75 (2008).

[36] Y. Mishin, Adaptive multiresolution methods for problems of computational geodynamics, PhD thesis, ETH Zürich, 2011.

[37] D. A. May, J. Brown, and L. Le Pourhiet, pTatin3d: High-performance methods for long-term lithospheric dynamics, 2014.

[38] L. C. Wilcox, G. Stadler, C. Burstedde, and O. Ghattas, A high-order discontinuous Galerkin method for wave propagation through coupled elastic-acoustic media, J. Comput. Phys. **229**(24), 9373–9396 (2010).

[39] C. R. Dohrmann and P. B. Bochev, A stabilized finite element method for the Stokes problem based on polynomial pressure projections, Int. J. Numer. Meth. Fluids **46**(2), 183–201 (2004).

[40] P. Bochev, C. Dohrmann, and M. Gunzburger, Stabilization of low-order mixed finite elements for the stokes equations, SIAM J. Numer. Anal. **44**(1), 82–101 (2006).

[41] C. Burstedde, O. Ghattas, G. Stadler, T. Tu, and L. C. Wilcox, Parallel scalable adjoint-based adaptive solution of variable-viscosity Stokes flow problems, Comput. Method. Appl. M. **198**(21–26), 1691–1700 (2009).

[42] M. Feistauer, J. Felcman, and I. Straškraba, Mathematical and Computational Methods for Compressible Flow (Oxford University Press, 2003).

[43] B. Cockburn and C. Shu, The Local Discontinuous Galerkin Method for Time-Dependent Convection-Diffusion Systems, SIAM J. Numer. Anal. **35**(6), 2440–2463 (1998).

[44] M. J. Guillot, B. Rivière, and M. F. Wheeler, Discontinuous Galerkin methods for mass conservation equations for environmental modelling, Dev. Water Sci. **47**, 939–946 (2002).

[45] M. Feistauer and V. Kučera, On a Robust Discontinuous Galerkin Technique for the Solution of Compressible Flow, J. Comput. Phys. **224**(1), 208–221 (2007).

[46] J. Aarnes and B. O. Heimsung, Multiscale Discontinuous Galerkin Methods for Elliptic Problems with Multiple Scales, in: Multiscale Methods in Science and Engineering, edited by B. Engquist, P. Lötstedt, and O. Runborg, Lecture Notes in Computational Science and Engineering Vol. 44 (Springer, 2005), pp. 1–20.

[47] N. K. Burgess and D. J. Mavriplis, hp-Adaptive Discontinuous Galerkin Solver for the Navier-Stokes Equations, AIAA J. **50**(12), 2682–2694 (2012).

[48] S. Giani, High-order/hp-adaptive discontinuous Galerkin finite element methods for acoustic problems, Computing **95**(1), 215–234 (2013).

[49] A. Baggag, H. Atkins, and D. Keyes, Parallel Implementation of the Discontinuous Galerkin Method, Tech. rep., Institute for Computer Applications in Science and Engineering (ICASE), 1999.

[50] H. Luo, L. Luo, A. Ali, R. Nourgaliev, and C. Cai, A Parallel, Reconstructed discontinuous Galerkin method for the compressible flows on arbitrary grids, Commun. Comput. Phys. **9**(2), 363–389 (2011).

[51] B. Cockburn, G. E. Karniadakis, and C. W. Shu (eds.), Discontinuous Galerkin Methods: Theory, Computation, and Applications, Lecture Notes in Computational Science and Engineering, Vol. 11 (Springer, 2000).

[52] D. N. Arnold, F. Brezzi, B. Cockburn, and L. D. Marini, Unified Analysis of Discontinuous Galerkin Methods for Elliptic Problems, SIAM J. Numer. Anal. **39**(5), 1749–1779 (2002).

[53] V. Etienne, E. Chaljub, J. Virieux, and N. Glinsky, An hp-adaptive discontinuous Galerkin finite-element method for 3-D elastic wave modelling, Geophys. J. Int. **183**(2), 941–962 (2010).

[54] D. Pageot, S. Operto, M. Vallée, R. Brossier, and J. Virieux, A parametric analysis of two-dimensional elastic full waveform inversion of teleseismic data for lithospheric imaging, Geophys. J. Int. **193**(3), 1479–1505 (2013).

[55] B. Cockburn, G. Kanschat, and D. Schötzau, A Note on Discontinuous Galerkin Divergence-free Solutions of the Navier-Stokes Equations, J. Sci. Comput. **31**(1–2), 61–73 (2007).

[56] V. J. Ervin, Computational bases for RT_k and BDM_k on triangles, Comput. Math. Appl. **64**(8), 2765–2774 (2012).

[57] Z. Cai and S. Zhang, Mixed methods for stationary Navier-Stokes equations based on pseudostress-pressure-velocity formulation, Math. Comput. **81**(280), 1903–1927 (2012).

[58] D. Griffiths and D. Silvester, Unstable modes of the Q1-P0 element, MIMS EPrint 2011.44, Manchester Institute for Mathematical Sciences, University of Manchester, Manchester, UK, 2011, This item originally appeared as MCCM Report 257 in 1994.

[59] P. Raviart and J. Thomas, A Mixed Finite Element Method for 2-nd Order Elliptic Problems, in: Mathematical Aspects of Finite Element Methods, edited by I. Galligani and E. Magenes, Lecture Notes in Mathematics Vol. 606 (Springer, 1977), chap. 19, pp. 292–315.

[60] G. Kanschat, Divergence-free Discontinuous Galerkin Schemes for the Stokes Equations and the MAC Scheme, Int. J. Numer. Meth. Fluids **56**(7), 941–950 (2008).

[61] F. Brezzi, J. Douglas Jr, and L. D. Marini, Two Families of Mixed Finite Elements for Second Order Elliptic Problems, Numer. Math. **47**(2), 217–235 (1985).

[62] F. Brezzi and M. Fortin, Mixed and Hybrid Finite Element Methods (Springer, New York, NY, USA, 1991).

[63] D. Braess, Finite Elements: Theory, Fast Solvers, and Applications in Solid Mechanics, 3rd edition (Cambridge University Press, 2007).

[64] M. F. Wheeler, An Elliptic Collocation-Finite Element Method with Interior Penalties, SIAM J. Numer. Anal. **15**(1), 152–161 (1978).

[65] D. A. Di Pietro and A. Ern, Mathematical Aspects of Discontinuous Galerkin Methods, Mathématiques et Applications, Vol. 69 (Springer, Berlin, 2012).

[66] M. Larson and F. Bengzon, The Finite Element Method: Theory, Implementation and Applications (Springer, 2013).

[67] J. Nečas, Direct Methods in the Theory of Elliptic Equations (Springer, 2012).

[68] J. T. Oden, I. Babuška, and C. E. Baumann, A Discontinuous hp Finite Element Method for Diffusion Problems, J. Comput. Phys. **146**(2), 491–519 (1998).

[69] C. Dawson, S. Sun, and M. F. Wheeler, Compatible algorithms for coupled flow and transport, Comput. Method. Appl. M. **193**(23–26), 2565–2580 (2004).

[70] D. N. Arnold, An interior penalty finite element method with discontinuous elements, SIAM J. Numer. Anal. **19**(4), 742–760 (1982).

[71] B. Rivière, M. F. Wheeler, and V. Girault, Improved energy estimates for interior penalty, constrained and discontinuous Galerkin methods for elliptic problems. Part I, Comput. Geosci. **3**(3-4), 337–360 (1999).

[72] F. Brezzi, G. Manzini, D. Marini, P. Pietra, and A. Russo, Discontinuous Galerkin approximations for elliptic problems, Numer. Meth. Part. D. E. **16**(4), 365–378 (2000).

[73] Z. Chen and H. Chen, Pointwise Error Estimates of Discontinuous Galerkin Methods with Penalty for Second-Order Elliptic Problems, SIAM J. Numer. Anal. **42**(3), 1146–1166 (2004).

[74] B. Rivière, Discontinuous Galerkin Methods For Solving Elliptic And Parabolic Equations: Theory and Implementation (Society for Industrial and Applied Mathematics, Philadelphia, PA, USA, 2008).

[75] B. Cockburn, G. Kanschat, and D. Schötzau, A locally conservative LDG method for the incompressible Navier-Stokes equations, Math. Comput. **74**(251), 1067–1095 (2005).

[76] J. Li and S. Sun, The Superconvergence Phenomenon and Proof of the MAC Scheme for the Stokes Equations on Non-uniform Rectangular Meshes, J. Sci. Comput. pp. 1–22 (2014).

[77] S. Zhong, Analytic Solutions for Stokes' Flow with Lateral Variations in Viscosity, Geophys. J. Int. **124**(1), 18–28 (1996).

[78] H. Ramberg, Instability of Layered Systems in the Field of Gravity, Phys. Earth Planet. Inter. **1**(7), 427–447 (1968).